International Journal of Minerals, Metallurgy and Materials
Volume 28, Number 1, January 2021, Page 150
https://doi.org/10.1007/s12613-020-2131-z

Sn/Sn_3O_{4-x} heterostructure rich in oxygen vacancies with enhanced visible light photocatalytic oxidation performance

Rui-qi Yang[1),*], *Na Liang*[1),*], *Xuan-yu Chen*[1)], *Long-wei Wang*[1)], *Guo-xin Song*[1)], *Yan-chen Ji*[1)], *Na Ren*[1)], *Ya-wei Lü*[2)], *Jian Zhang*[3)], *and Xin Yu*[1)]

1) Institute for Advanced Interdisciplinary Research (IAIR), University of Jinan, Jinan 250022, China
2) School of physics and electronics, Hunan University, Changsha 410082, China
3) Institute Charles Gerhardt, UMR 5253, CNRS-UM-ENSCM, Université de Montpellier, Place Eugène Bataillon, F-34095 Montpellier cedex 5, France
(Received: 20 April 2020; revised: 24 June 2020; accepted: 30 June 2020)

Abstract: Sn_3O_4, a common two-dimensional semiconductor photocatalyst, can absorb visible light. However, owing to its rapid recombination of photogenerated electron−hole pairs, its absorption is not sufficient for practical application. In this work, a Sn nanoparticle/Sn_3O_{4-x} nanosheet heterostructure was prepared by *in situ* reduction of Sn_3O_4 under a H_2 atmosphere. The Schottky junctions formed between Sn and Sn_3O_{4-x} can enhance the photogenerated carrier separation ability. During the hydrogenation process, a portion of the oxygen in the semiconductor can be extracted by hydrogen to form water, resulting in an increase in oxygen vacancies in the semiconductor. The heterostructure showed the ability to remove Rhodamine B. Cell cytocompatibility experiments proved that Sn/Sn_3O_{4-x} can significantly enhance cell compatibility and reduce harm to organisms. This work provides a new method for the fabrication of a Schottky junction composite photocatalyst rich in oxygen vacancies with enhanced photocatalytic performance.

Keywords: photocatalysis; tin oxide; oxygen vacancy; Schottky junction; photodegradation

1. Introduction

Water pollution is the most serious problem affecting the environment, reducing the value of water and threatening human survival [1]. Organics are the most important factor causing water pollution, mainly due to their difficulty for biodegradation, long-term residue, and high toxicity [2−4]. There are many limitations of traditional wastewater treatment methods, for example, biological treatment technologies do not completely degrade organics, and physical and chemical treatment technologies are less efficient for contaminant removal and may cause secondary pollution [5−6]. In 1972, Japanese scholars Fujishima and Honda [7] discovered that a titanium dioxide (TiO_2) semiconductor can photoelectrocatalyze the decomposition of water to produce hydrogen (H_2) and oxygen (O_2). The photocatalytic redox technology of nanostructured semiconductors has broad application prospects for wastewater treatment [8−11], air purification [12], and antibacterial photocatalytic therapy [13−15]. Photocatalytic technology has widespread interest and a period of rapid development. In the last decade, the technology has been demonstrated to have strong advantages in addressing water pollution [16−19].

The potential advantages of the photocatalytic oxidation treatment of pollutants are mainly: (1) The utilization of solar energy by designing visible light or even full-spectrum catalysts can significantly improve the catalyst degradation efficiency and reduce costs [20−22]; (2) Dye, pesticide, oil, and other organic pollutants can be effectively degraded and eventually completely mineralized into carbon dioxide, water, and other inorganic molecular substances through photocatalysis [23−26]; (3) Polluting additives are not needed and no toxic intermediates are produced. Unfortunately, most single-phase photocatalysts exhibit low catalytic activity due to a high photogenerated carrier recombination efficiency and poor light absorption capacity [27]. Therefore, the design of highly efficient photocatalytic materials is the core requirement of photocatalytic technologies.

*These authors contributed equally to this work.

Corresponding authors: Na Ren E-mail: bio_renn@ujn.edu.cn; Ya-wei Lü E-mail: lyyawei@hnu.edu.cn;
Xin Yu E-mail: ifc_yux@ujn.edu.cn

In recent decades, transition metal oxide semiconductors have been widely used in the field of photocatalysis [28−30]. Previous works have confirmed that Sn_3O_4 (the band gap is nearly 2.70 eV) can absorb visible light to catalyze organic pollutant degradation [31−32]. However, pure Sn_3O_4 still has some unavoidable defects that limit its use: (1) The range of visible light absorption is limited (<500 nm), which reduces the solar energy utilization; (2) The photocatalytic stability and performance of pure Sn_3O_4 are not satisfactory due to poor charge separation and a high recombination rate of photogenerated electron and hole pairs; (3) Sn_3O_4 has poor catalytic kinetics, the photocatalytic performance of Sn_3O_4 is highly dependent on a precious metal cocatalyst, which has cost constraints. Therefore, a simple and low-cost method to expand the absorption spectrum range, promote carrier separation, and improve reaction kinetics is essential to improving the photocatalytic activity of pure Sn_3O_4. Balgude *et al.* [33] reported a layered Sn_3O_4 with good photodegradation performance under sunlight irradiation. Li *et al.* [34] synthesized Z-scheme mes-Sn_3O_4/g-C_3N_4 heterostructures for efficiently removing tetracycline hydrochloride (TC-HCl) from water. Zhu *et al.* [35] synthesized three-dimensional (3D) TiO_2/Sn_3O_4 heterostructure arrays that can act as a photoanode with excellent photoelectrochemical H_2 generation activity. Our recent work demonstrated that a Sn_3O_4/nickel foam hierarchical nanostructure can utilize the full spectrum to efficiently degrade polyacrylamide [36]. Recently, it was reported that the photocatalytic activity can be significantly enhanced by introducing oxygen vacancies into materials [37−39]. In particular, surface oxygen vacancies can capture and transfer photogenerated carriers to the photocatalyst surface rapidly, thus effectively preventing the recombination [40]. More specifically, the introduction of oxygen vacancies into the catalyst reduces the coordination number of adjacent catalytic sites and adjusts the surface electronic structure, thereby affecting the inherent catalytic activity [41]. Oxygen vacancies will also induce an outward hole trapping force and drive the migration of holes, thereby promoting the separation of photogenerated electrons and holes [42]. In addition, since nanometals have good conductivity, a Schottky barrier can be formed between metal and semiconductor interfaces. Studies have shown that the photocatalytic ability can be remarkably enhanced by introducing metal nanoparticles on the surface of a semiconductor photocatalyst [43].

In this work, we synthesized a Sn/Sn_3O_{4-x} heterostructure with oxygen vacancies by *in situ* reduction of Sn_3O_4 under a H_2 atmosphere. The excellent conductivity of Sn metal and the interaction of the metal–semiconductor interface promoted the separation and transport of the photogenerated carriers. Furthermore, the presence of oxygen vacancies in Sn_3O_{4-x} can inhibit the recombination of photogenerated carriers. Thus, Sn/Sn_3O_{4-x} exhibited better photodegradation performance than pure Sn_3O_4, and a photocatalyst with the highest photocatalytic performance can be produced by controlling the calcination time and temperature. The cell cytocompatibility experiments of Sn/Sn_3O_{4-x} confirmed the toxicity of Sn_3O_4 can be significantly reduced. This work provides a favorable method for constructing a low-cost Schottky junction composite photocatalyst rich in oxygen vacancies with enhanced photocatalytic oxidation performance.

2. Experimental

2.1. Synthesis of Sn_3O_4 nanosheets

In a typical experiment, 7.35 g of trisodium citrate dihydrate ($Na_3C_6H_5O_7·2H_2O$) and 2.256 g of tin(II) chloride dihydrate ($SnCl_2·2H_2O$) were dissolved in deionized water (50 mL). Under constant stirring, 25 mL of 0.2 M sodium hydroxide (NaOH) was added and stirred until a clear solution was obtained. The solution was transferred to a Teflon-lined stainless-steel autoclave (100 mL) and heated to 190°C for 10 h to produce the Sn_3O_4 nanosheets.

2.2. Synthesis of the Sn/Sn_3O_{4-x} heterostructure

Sn/Sn_3O_{4-x} nanocomposites were prepared by reduction of Sn_3O_4 nanosheets under a H_2 atmosphere in a quartz tube. The experimental conditions for the fabrication of the 400-5, 400-30, 500-5, and 500-30 samples are listed in Table 1.

Table 1. Experimental conditions of the Sn/Sn_3O_{4-x} samples

Sample	Calcination temperature / °C	Calcination time / min
400-5	400	5
400-30	400	30
500-5	500	5
500-30	500	30

2.3. Characterization

Scanning electron microscopy (SEM) equipped with energy-dispersive X-ray (EDX) spectroscopy (Hitachi SU8020, Japan) and high-resolution transmission electron microscopy (HRTEM, FEI/Tecnai G2 F20, USA) were used to characterize the morphology of the nanomaterials. The crystal structure of the samples was characterized by X-ray diffraction (XRD) using the powder X-ray diffractometer (Bruker D8 Advance, Germany) with Cu K_α radiation (wavelength λ = 0.15406 nm). The ultraviolet−visible diffuse reflectance spectra (UV−Vis DRS) of the nanomaterials were analyzed on a UV−Vis spectrophotometer (Hitachi UH4150, Japan). Raman spectra measurements were collected with a confocal microscopic Raman spectrometer (Horiba, LabRAM HR Evdution, France) equipped with an argon ion laser (532 nm). X-ray photoelectron spectroscopy (XPS) was obtained by a X-ray photoelectron spectrometer (Kratos Axis ultra-DLD, UK) with a monochromatized Mg K_α X-ray source (energy $h\nu$ = 1283.3 eV). The binding energies were normalized to the signal for adventitious carbon at 284.6 eV.

2.4. Photoelectrochemical measurement

Photoelectrochemical (PEC) testing was performed using an electrochemical workstation (CHI 660E, CH Instrument, China). For synthesis of the working electrodes, the synthesized catalysts were mixed with terpineol for 10 h to form a slurry with the same concentration, and the slurries were then coated on clean fluorine-doped tin oxide (FTO) glass and dried at 80°C. In order to form a good electrical connection between the catalyst and FTO substrate, the electrodes were heated to 250°C for 2 h under an Ar atmosphere. In a typical PEC testing, a standard three electrode cell were used: reference electrode (saturated calomel electrode), counter electrode (platinum sheet), and work electrode (FTO with the photocatalyst). The electrolyte was a 0.5 M sodium sulfate solution (pH = 6.8). A 300 W xenon lamp (AM 1.5 G filter, 100 mW·cm^{-2}) was used as the light source.

2.5. Photocatalytic degradation performance

The decomposition process of a Rhodamine B (Rh B) aqueous solution was monitored to evaluate the photodegradation performance of the different samples. The experiment was conducted in a photochemical reaction system (CEL-LAB500E5, China Education Au-Light Co., Ltd.). The Rh B solution (10 ppm, 20 mL) was mixed with 20 mg of the samples, and in a dark condition, the solution was stirring for 30 min to achieve adsorption−desorption equilibrium. A 300 W xenon lamp (AM 1.5 G filter) equipped with a cutoff filter to remove light with wavelength λ < 420 nm was used for illumination. The absorption spectrum of the samples were measured at certain intervals under light to obtain the degradation rate.

2.6. Cytotoxicity evaluation

50 mg of the Sn_3O_4 and Sn/Sn_3O_{4-x} heterostructure were immersed in cell culture medium (20 mL) for 1 d. Cells were seeded in 48-well plates at 2×10^4 cells/well and were incubated at 37°C for 1 d. Culture medium was added to the wells after washing the cells with phosphate buffered saline (PBS). Fresh media containing Cell Counting Kit-8 solution (10vol%) was used to replace the culture medium and quantitatively evaluate the cell viability. Finally, a fluorescent microscope was used to observe the cells.

3. Results and discussion

3.1. Theoretical calculation

The molecular structures of Sn_3O_4 and Sn_3O_4 with oxygen vacancy (Sn_3O_{4-x}) and corresponding band structures are shown in Fig. 1. The hydrogenation process leads to partial oxygen loss in the semiconductor to form water, resulting in increased oxygen vacancies in Sn_3O_{4-x}. Compared to Sn_3O_4, the higher valence band (VB) top and the lower conduction band (CB) bottom cause Sn_3O_{4-x} to have a smaller band gap, which is conducive to improving solar energy utilization. In addition, the confusion degree of Sn_3O_{4-x} increases compared with Sn_3O_4, indicating the formation of a defect state, which is also advantageous to the enhancement of photocatalytic activity.

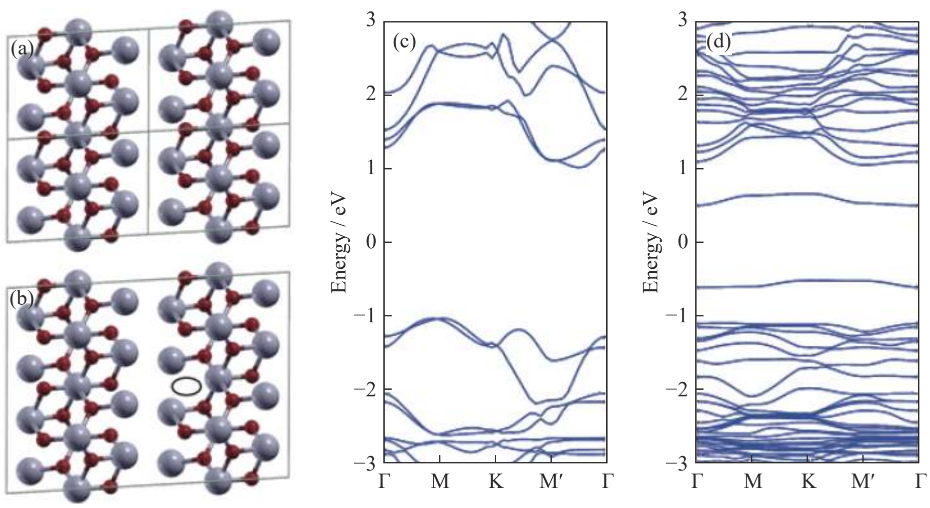

Fig. 1. Optimized geometry structures of (a) Sn_3O_4 and (b) Sn_3O_{4-x} (Gray and red balls represent Sn and O, respectively); band structures of (c) Sn_3O_4 and (d) Sn_3O_{4-x}.

3.2. Characterization of the photocatalysts

The process to prepare Sn/Sn_3O_{4-x} is illustrated in Fig. 2(a). The first step is to synthesize Sn_3O_4 nanosheets (NSs) using a facile hydrothermal method, and the second step is to reduce the synthesized Sn_3O_4 sample in a tube furnace under a H_2 atmosphere at a determined calcination temperature and time to produce the Sn/Sn_3O_{4-x} heterostructure. As shown in the SEM images of Figs. 2(b) and 2(c), the Sn_3O_4 material was a 3D flower-like aggregate assembled from many nanosheets. When hydrogenation was performed at a lower temperature of 400°C, the morphology of 400-5 and 400-30 did not obviously change due to the low reduction. As the reduction degree increased with increasing temperature, the nanosheets gradually transformed into nanoparticles. As shown in Figs. 2(d) and 2(e), after reduction at 500°C for 5 min, Sn nanoparticles with diameters of 100–200 nm were dispersed on the surface of Sn_3O_4 nanosheets. As the reduction time increased to 30 min, Sn_3O_4 was completely converted to Sn nanoparticles. The diameters of the Sn nanoparticles were 100–300 nm (Figs. 2(f) and 2(g)). The EDS element mapping results in Fig. 2(h) also confirmed the existence of O and Sn, indicating partial reduction of Sn_3O_4 to Sn in the 500-5. Figs. 2(i) and 2(j) show typical TEM images

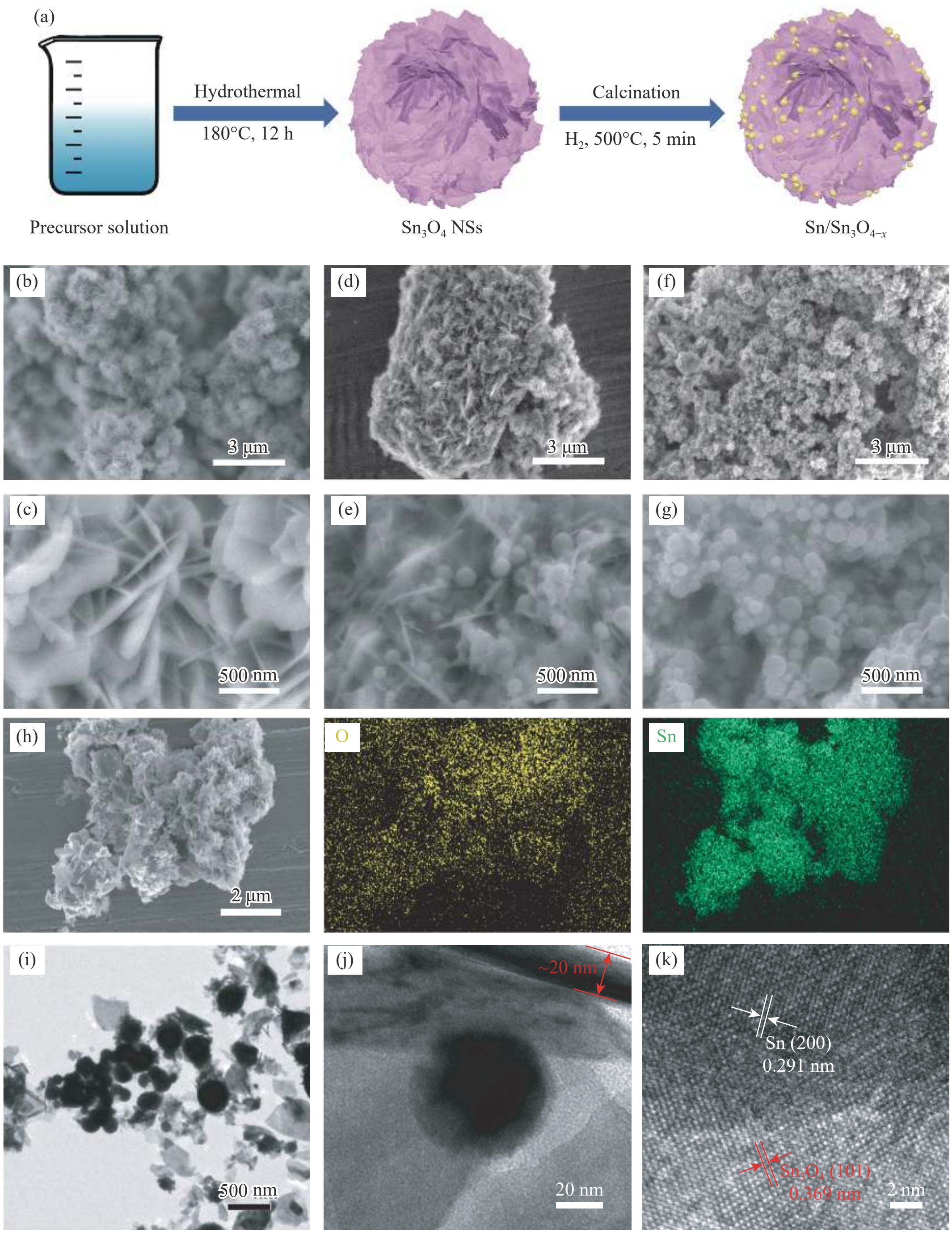

Fig. 2. (a) Schematic diagram of the synthetic process of the Sn/Sn_3O_{4-x} heterostructure; typical SEM images of the (b, c) Sn_3O_4 nanosheets, (d, e) 500-5, and (f, g) 500-30; (h) EDS element mapping of 500-5; (i, j) TEM and (k) HRTEM images of 500-5.

of the 500-5 nanostructure. The Sn_3O_4 nanosheets were interlaced with Sn nanoparticles, coinciding with SEM observations. Additionally, as shown in Fig. 2(j), the thickness of the Sn_3O_4 nanosheet was approximately 20 nm. Furthermore, the HRTEM image of the 500-5 displayed two types of lattice fringes (Fig. 2(k)). The interplanar spacing of 0.369 nm corresponds to the (101) crystal orientation of Sn_3O_4 and the other interplanar spacing of 0.291 nm is the (200) crystal orientation of Sn [44].

The crystal phases of the different samples were analyzed using XRD. As shown in Fig. 3(a), the diffraction peaks of Sn_3O_4 were consistent with the standard triclinic-phase (JCPDS card, No. 16-0737) [45]. With the reduction degree increasing, the diffraction peaks of Sn_3O_4 gradually weakened, and the peaks of Sn appeared and gradually increased. For 500-30, the diffraction peaks at 30.6°, 32.0°, 43.8°, 44.9°, 55.3°, 62.5°, 63.7°, 64.5°, 72.4°, 73.1°, and 79.4° corresponded to the (200), (101), (220), (211), (301), (112), (400), (321), (421), (411), and (312) crystal faces of Sn (JCPDS card, No. 04-0673) [46]. For the 400-4, 400-30, and 500-5 samples, all of the diffraction peaks were indexed to Sn or Sn_3O_4. The Raman spectrum of Sn_3O_4, 400-5, 400-30, 500-5, and 500-30 shown in Fig. 3(b) clearly showed peaks for Sn_3O_4 at approximately 71, 83, 137, 166, and 236 cm^{-1} [47]. As the reduction degree increased, the peaks of Sn_3O_4 gradually weakened and disappeared, indicating conversion of Sn_3O_4 to Sn. In addition, UV−Vis DRS was used to characterized the light absorption properties of the samples (Fig. 3(c)). Sn_3O_4 exhibits the absorption ability in the visible light region with an approximate 480 nm cutoff edge. After forming the Sn/Sn_3O_{4-x} heterostructure, the light absorption range significantly increased to the entire wavelength and the light absorption intensity was also enhanced. The increase in the light absorption range is mainly due to the formation of Sn metal particles. The red shift of the absorption improves the light harvesting ability, which contributes to the enhanced photocatalytic activity.

The surface electronic states and chemical composition of the Sn_3O_4 and 500-5 were determined by XPS. Form Fig. 4(a), the characteristic peaks of 500-5 shifted to a lower binding energy compared with Sn_3O_4, which means an increase in electron density. For 500-5, Sn 3d can obtain three characteristic peaks by curve fitting, the peaks near 495.1 and 486.6 eV were well indexed to Sn(IV) and the peaks at 494.4 and 485.8 eV corresponded to Sn(II), whereas those at 493.1 and 484.6 eV were related to Sn(0). The Sn 3d region of Sn_3O_4 was fitted to the peaks corresponding to Sn(IV) at 495.2 and 486.7 eV and Sn(II) at 494.6 and 486.0 eV. There was no Sn(0) peak. This indicates that Sn was successfully introduced into the 500-5 sample through the H_2 reduction process. As shown in Fig. 4(b), the O 1s can be fitted to three characteristic peaks in Sn_3O_4 and 500-5. Specifically, the O1 peak may be caused by oxygen atoms bound to metals, the O3 peak is attributed to the hydroxy species of surface-adsorbed water molecules, and the O2 peak is due to defect sites with low oxygen coordination, indicating the existence of oxygen vacancies [41].

Furthermore, electron paramagnetic resonance (EPR) testing was conducted at room temperature to further demonstrate the formation of oxygen vacancies after a H_2 atmo-

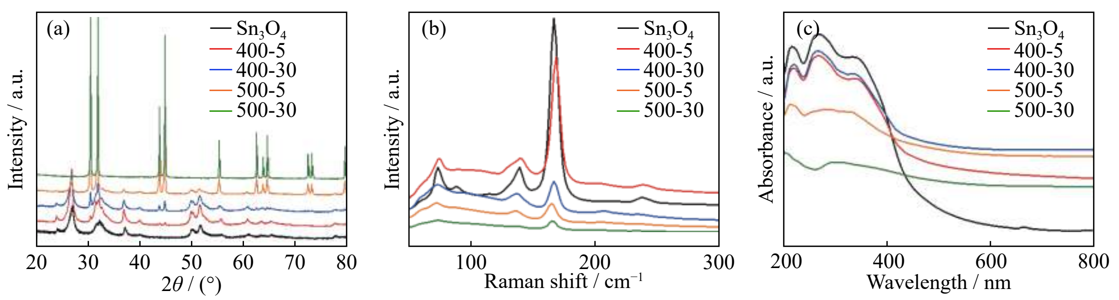

Fig. 3. (a) XRD pattern, (b) Raman spectra, and (c) UV−Vis diffuse reflectance spectra of the different samples.

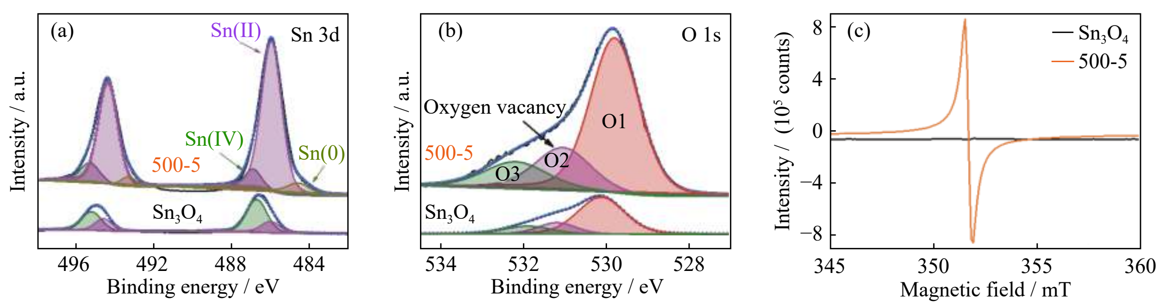

Fig. 4. High-resolution XPS of (a) Sn 3d and (b) O 1s spectra of Sn_3O_4 and 500-5; (c) EPR spectra of Sn_3O_4 and 500-5 at room temperature.

sphere reduction. As shown in Fig. 4(c), no signal was detected in the pure Sn_3O_4. However, a single EPR signal belonging to the oxygen vacancies was clearly observed in 500-5. Therefore, EPR accurately confirmed the formation of oxygen vacancies in Sn/Sn_3O_{4-x}, which will contribute to improve the visible light-driven photocatalytic oxidation activity.

According to these results, Sn_3O_4 was successfully synthesized by a hydrothermal method. Reduction under a H_2 atmosphere was a temperature and time control process, and hydrogenation enabled Sn_3O_{4-x} to obtain surface oxygen vacancies. Simultaneously, the Sn/Sn_3O_{4-x} obtained by calcination at 500°C for 5 min had an excellent light absorption capacity.

3.3. Photoelectrochemical performance

Tauc plots were used to further analyze the light absorption properties (Fig. 5(a)). The indirect bandgap of the different photocatalysts can be calculated from the DRS using the Kubelka–Munk (K–M) method with the following formula [48]:

$$\alpha h\nu = A(h\nu - E_g)^2 \quad (1)$$

where $h\nu$ is the photon energy, α is the absorption coefficient, E_g is the indirect band gap, and A is a constant. Using Eq. (1), the E_g values of pure Sn_3O_4 and 500-5 were approximately 2.82 and 2.6 eV, respectively. The decrease in the bandgap indicates the absorption performance improves.

The instant photocurrent density of the samples was measured to further explain the improvement in the photocatalytic oxidation performance of Sn/Sn_3O_{4-x}. Fig. 5(b) shows a relatively low photocurrent density (approximately 0.32 $\mu A\cdot cm^{-2}$) of pure Sn_3O_4 under the continuous alternating switching light illumination. The photocurrent densities of 400-5 and 400-30 were 0.51 and 0.53 $\mu A\cdot cm^{-2}$, respectively. It is worth noting that 500-5 showed a maximum photocurrent density of approximately 0.65 $\mu A\cdot cm^{-2}$. The 500-30 sample was Sn metal after the complete reduction of Sn_3O_4, the current was not enhanced under light, and the sample had the largest current density due to excellent conductivity. The enhanced photocurrent density of Sn/Sn_3O_{4-x} is attributed to the enhanced separation efficiency of the photogenerated carriers due to the formation of a Schottky junction at the Sn and Sn_3O_{4-x} interface and the presence of surface oxygen vacancies in Sn_3O_{4-x}.

Electrochemical impedance spectra (EIS) are a powerful tool for assessing surface charge transport resistance. The smaller the radius, the lower the charge transfer resistance, which facilitates the transfer of charges [49]. The Nyquist plots of the samples were measured at an open circuit voltage as shown in Fig. 5(c). Compared with the other samples, the 500-5 sample showed the smallest radius, indicating that it had the lowest carrier transport resistance, which is beneficial to the rapid transmission of photogenerated carriers at the interface. These results further indicate that 500-5 had the best photocatalytic performance. The photoelectrochemical analysis indicates that the enhancement of the photocatalytic oxidation ability of Sn/Sn_3O_{4-x} is attributed to the Schottky junction, which allows more carriers to be quickly transferred to the catalyst surface to participate in the oxidation reaction.

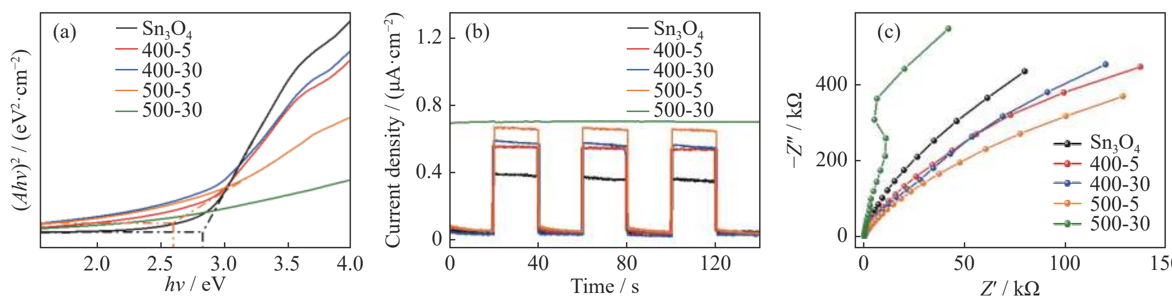

Fig. 5. (a) Tauc plots of the synthetic catalysts; (b) instant photocurrent responses at 0 V vs. SCE bias of the different samples; (c) EIS Nyquist plots of synthesized catalysts measured at open circuit voltage (Impedance is a complex number, *Z'* and *Z"* represent real and imaginary parts, respectively).

3.4. Photodegradation activity

As shown in Fig. 6, the photocatalytic oxidation activity was evaluated by performing degradation experiments of Rh B under visible light. The degradation degree was assessed through the maximum absorption peak at 554 nm of Rh B. By measuring the light absorption, the concentrations of Rh B at time t (C_t) and time t = 0 (C_0) could be calculated. The efficiency of photodegradation can be determined by calculating the value of C_t/C_0 [50]. Fig. 6(a). shows the degradation curves of Rh B under visible light irradiation of the Sn_3O_4, 400-5, 400-30, 500-5, and 500-30. The photodegradation of Rh B by pure Sn_3O_4 was weak and the degradation rate after 1 h was only 9%. After H_2 reduction at a certain calcination temperature and time to obtain Sn/Sn_3O_{4-x}, the degradation efficiency was improved, indicating that the formation of the junction between the metal Sn and semiconductor

Sn_3O_{4-x} is beneficial for enhancing the photocatalytic oxidation performance. When the reduction temperature was 500°C, 500-5 obtained for 5 min had the best photocatalytic performance and the degradation rate reached 39% after 1 h. Fig. 6(b) shows the absorption spectra of Rh B degraded by 500-5 under different irradiation times. As the time increases, the maximum absorption peak of Rh B gradually decreases, indicating that Rh B was continuously degraded under visible light irradiation. To further understand the degradation process, the photocatalytic degradation kinetics of Rh B with the different samples were analyzed. The degradation follows the pseudo first-order kinetics equation [51]:

$$\ln (C_t/C_0) = -at \quad (2)$$

where t and a represent the time and kinetic constant, respectively.

In Figs. 6(c) and 6(d), the fitting curves shows that kinetic constant was only 0.0018 min^{-1} with Sn_3O_4 for Rh B removal, while the kinetic constant improved after the formation of Sn/Sn_3O_{4-x} by H_2 reduction. The kinetic constant of the 400-5 was 0.0035 min^{-1}, and 400-30 was 0.0032 min^{-1}. For 500-5, the kinetic constant was up to 0.0069 min^{-1}, which was approximately 3.8 times greater than that of pure Sn_3O_4. The a of 500-30 was 3.8×10^{-4} min^{-1}, which was nearly negligible. The 500-30 sample was obtained by calcining at 500°C for 30 min, Sn_3O_4 was nearly completely converted to metal Sn based on the XRD results, such that it had the lowest photocatalytic activity and nearly no degradation effect on Rh B.

To confirm the photocatalytic degradation mechanism, degradation experiments with different trapping agents were performed. In photocatalytic systems, hydroxyl radicals (·OH), superoxide radicals ($\cdot O_2^-$), and holes (h^+) are generally regarded as active species that will eventually oxidize organic pollutants. Fig. 7 exhibits the degradation of Rh B by the Sn/Sn_3O_{4-x} heterostructure under light for 1 h after adding tert-butanol (TBA), ammonium oxalate (AO), and p-benzoquinone (BQ) to capture ·OH, h^+ and $\cdot O_2^-$, respectively. When AO was added, the degradation rate of Rh B slightly decreased. Notably, after the introduction of TBA or BQ, the degradation rate was severely suppressed, which indicates that $\cdot O_2^-$ and ·OH play a major role in the reaction system, and the photoexcited h^+ has the secondary impact.

3.5. Band structure of Sn/Sn_3O_{4-x}

The charge transfer process during photocatalytic degradation is proposed in Fig. 8. With visible light irradiation, Sn_3O_{4-x} can be excited and photogenerated electrons (e^-) generated with VB transport to the corresponding CB, thereby leaving photogenerated h^+ on the VB. Due to the formation of Schottky junctions at the metal/semiconductor interface and the presence of surface oxygen vacancies in Sn_3O_{4-x}, the e^- on

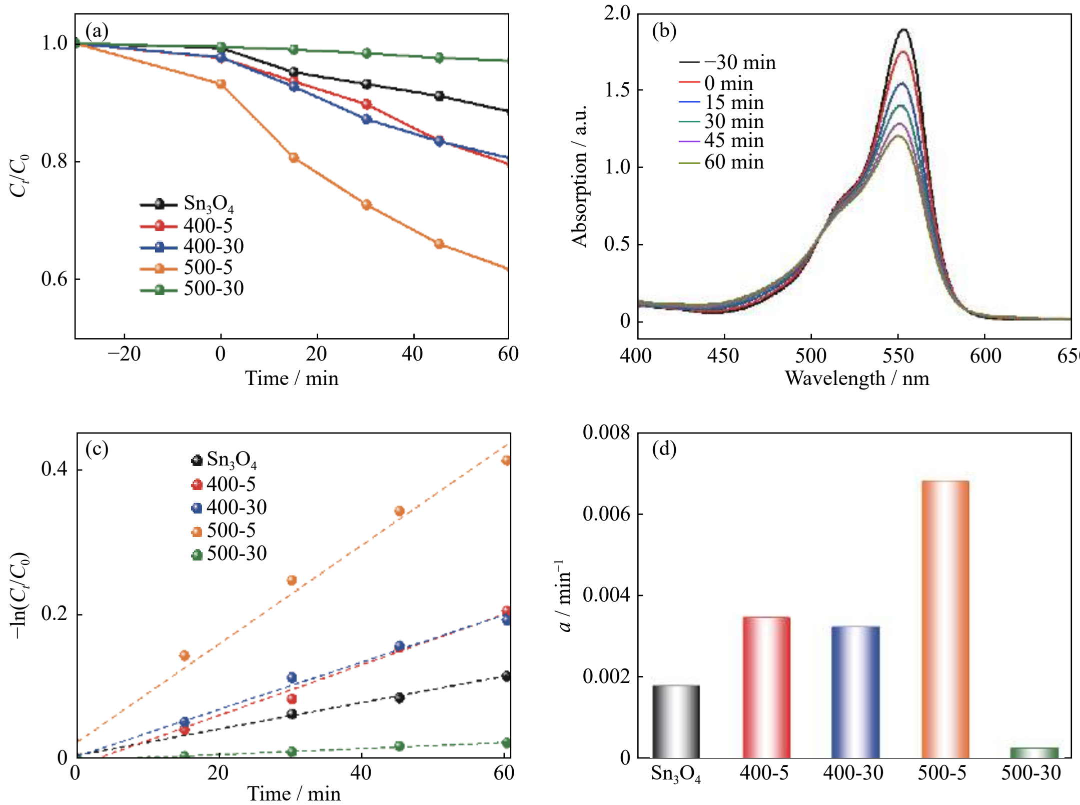

Fig. 6. (a) Degradation degrees of Rh B using Sn_3O_4, 400-5, 400-30, 500-5, and 500-30; (b) absorption spectra of Rh B solution with various time intervals during the degradation of Rh B by 500-5; (c) Kinetic curves of Rh B photocatalytic degradation of the different samples and (d) the corresponding reaction constants.

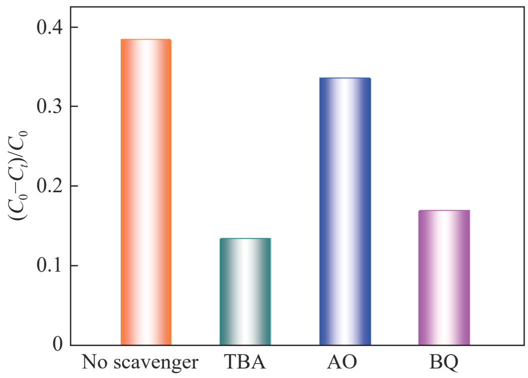

Fig. 7. Effects of various scavengers on the photocatalytic efficiencies of Sn/Sn_3O_{4-x} heterostructure for the degradation of Rh B under visible light irradiation.

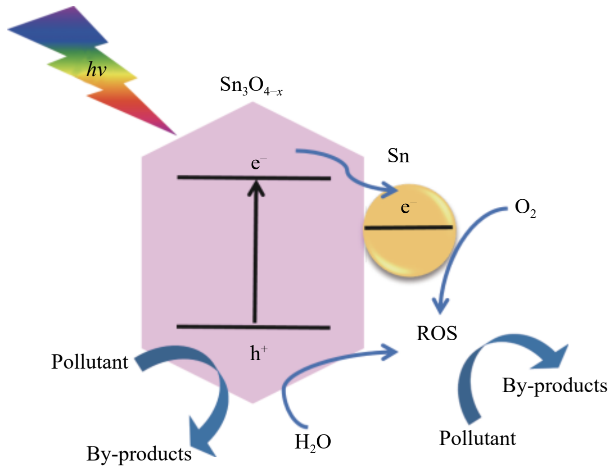

Fig. 8. Schematic diagram of the band structure and electron transfer (ROS stands for reactive oxygen species, including $\cdot O_2^-$, ·OH, etc.).

the CB of Sn_3O_{4-x} can be rapidly transferred to the Sn, thereby improving the separation efficiency of photogenerated carriers. Furthermore, the photoexcited e^- can react with dissolved oxygen to produce $\cdot O_2^-$, which can directly catalyze pollutants or further react with H^+ to form ·OH to oxidize organic contaminants. Additionally, light-excited h^+ can also react with H_2O to generate hydroxyl radicals (·OH) and play a small role.

3.6. Cytotoxicity evaluation

The above results confirmed that Sn/Sn_3O_{4-x} exhibited the best photocatalytic degradation activity. Furthermore, the cytotoxicity of synthetic Sn_3O_4 and Sn/Sn_3O_{4-x} to a human breast adenocarcinoma cell line, MCF-7, was assessed using LIVE/DEAD® Viability/Cytotoxicity Kit. In Fig. 9(a), the red dots indicate dead cells while the green regions indicate live cells. Compared with the control group without any catalyst, the culture medium treated with Sn_3O_4 showed significant cell death at 24 and 48 h, indicating that pure Sn_3O_4 has significantly toxicity to MCF-7 cells. Notably, the cells cultured in medium treated with Sn/Sn_3O_{4-x} survived well and showed significantly enhanced cytocompatibility compared with Sn_3O_4, which did not cause secondary harm to aquatic organisms. Next, Cell Counting Kit (CCK-8) was used to evaluate the viability of cells treated with different media, measuring the absorbance (OD) at the maximum absorption wavelength of 450 nm. The result is shown in Fig. 9(b), the medium treated with Sn/Sn_3O_{4-x} had little effect on the cell viability at 24 and 48 h, whereas the medium treated with Sn_3O_4 resulted in increased cell death. These results indicate that the Sn/Sn_3O_{4-x} obtained by *in situ* reduction successfully improved the material biocompatibility.

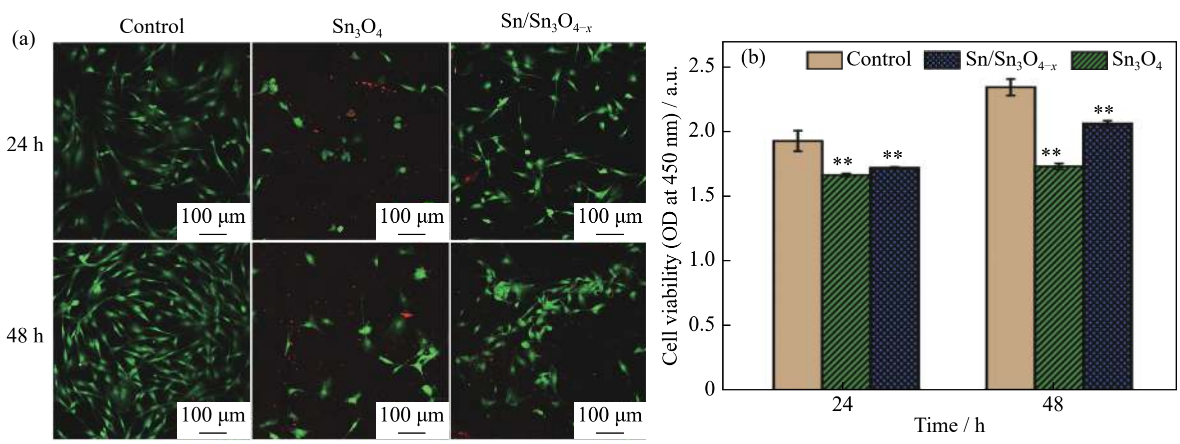

Fig. 9. Cytotoxicity of Sn/Sn_3O_{4-x} in MCF-7 cells: (a) live/dead cells staining of culture medium treated with Sn_3O_4 and Sn_3O_{4-x} for 24 and 48 h; (b) cell viability (The statistical significance is indicated by probability (*P*), and ** indicates $P < 0.01$).

4. Conclusion

A Sn/Sn_3O_{4-x} heterostructure was synthesized by hydrothermal method and *in situ* reduction under a H_2 atmosphere successfully, exhibiting significantly enhanced photodegradation under visible light irradiation. The 500-5 sample exhibited the best performance, which was acquired by controlling the calcination time and temperature. The enhanced photocatalytic oxidation activity of the heterostructure is attributed to the high conductivity and optical reflectivity of Sn metal, the abundant oxygen vacancies in Sn_3O_{4-x}, and the formation of a Schottky junction at the semiconductor/metal interface, which effectively improves the capacity of the light absorption and accelerates charge separation and transfer. Additionally, Sn/Sn_3O_{4-x} showed lower cytotoxicity than pure Sn_3O_4. This work provides a new strategy for low-cost Schottky junction composite photocatalysts rich in oxygen vacancies with excellent photocatalytic property.

Acknowledgements

This work was financially supported by the National Natural Science Foundation of China (Nos. 51802115 and 51732007) and the Natural Science Foundation of Shandong Province, China (No. ZR2019YQ21).

References

[1] O.M. Rodriguez-Narvaez, J.M. Peralta-Hernandez, A. Goonetilleke, and E.R. Bandala, Treatment technologies for emerging contaminants in water: A review, *Chem. Eng. J.*, 323(2017), p. 361.

[2] H. Rajbongshi and D. Kalita, Morphology-dependent photocatalytic degradation of organic pollutant and antibacterial activity with CdS nanostructures, *J. Nanosci. Nanotechnol.*, 20(2020), No. 9, p. 5885.

[3] X.Q. Liu, J. Iocozzia, Y. Wang, X. Cui, Y.H. Chen, S.Q. Zhao, Z. Li, and Z.Q. Lin, Noble metal-metal oxide nanohybrids with tailored nanostructures for efficient solar energy conversion, photocatalysis and environmental remediation, *Energy Environ. Sci.*, 10(2017), No. 2, p. 402.

[4] T.S. Galloway, M. Cole, and C. Lewis, Interactions of microplastic debris throughout the marine ecosystem, *Nat. Ecol. Evol.*, 1(2017), No. 5, art. No. 0116.

[5] G. Lofrano, S. Meriç, G.E. Zengin, and D. Orhon, Chemical and biological treatment technologies for leather tannery chemicals and wastewaters: A review, *Sci. Total Environ.*, 461-462(2013), p. 265.

[6] P.I. Cano, J. Colón, M. Ramírez, J. Lafuente, D. Gabriel, and D. Cantero, Life cycle assessment of different physical-chemical and biological technologies for biogas desulfurization in sewage treatment plants, *J. Cleaner Prod.*, 181(2018), p. 663.

[7] A. Fujishima and K. Honda, Electrochemical photolysis of water at a semiconductor electrode, *Nature*, 238(1972), No. 5358, p. 37.

[8] H.H. Wang, W.X. Liu, J. Ma, Q. Liang, W. Qin, P.O. Lartey, and X.J. Feng, Design of $(GO/TiO_2)_N$ one-dimensional photonic crystal photocatalytic photocatalysts with improved photocatalytic activities for tetracycline degradation, *Int. J. Miner. Metall. Mater.*, 27(2020), No. 6, p. 830.

[9] Y.C. Zhang, Q. Zhang, Z.Y. Dong, L.Y. Wu, and J.M. Hong, Degradation of acetaminophen with ferrous/copperoxide activate persulfate: Synergism of iron and copper, *Water Res.*, 146(2018), p. 232.

[10] P. Wang, S. Guo, H.J. Wang, K.K. Chen, N. Zhang, Z.M. Zhang, and T.B. Lu, A broadband and strong visible-light-absorbing photosensitizer boosts hydrogen evolution, *Nat. Commun.*, 10(2019), art. No. 3155.

[11] H.X. Liu, M.Y. Teng, X.G. Wei, T.D. Li, Z.Y. Jiang, Q.F. Niu, and X.P. Wang, Mosaic structure ZnO formed by secondary crystallization with enhanced photocatalytic performance, *Int. J. Miner. Metall. Mater.*(2020). DOI: 10.1007/s12613-020-2033-0

[12] M. Sansotera, S.G.M. Kheyli, A. Baggioli, C.L. Bianchi, M.P. Pedeferri, M.V. Diamanti, and W. Navarrini, Absorption and photocatalytic degradation of VOCs by perfluorinated ionomeric coating with TiO_2 nanopowders for air purification, *Chem. Eng. J.*, 361(2019), p. 885.

[13] X. Yu, S. Wang, X.D. Zhang, A.H. Qi, X.R. Qiao, Z.R. Liu, M.Q. Wu, L.L. Li, and Z.L. Wang, Heterostructured nanorod array with piezophototronic and plasmonic effect for photodynamic bacteria killing and wound healing, *Nano Energy*, 46(2018), p. 29.

[14] L.W. Wang, X. Zhang, X. Yu, F.E. Gao, Z.Y. Shen, X.L. Zhang, S.G. Ge, J. Liu, Z.J. Gu, and C.Y. Chen, An all-organic semiconductor C_3N_4/PDINH heterostructure with advanced antibacterial photocatalytic therapy activity, *Adv. Mater.*, 31(2019), No. 33, art. No. 1901965.

[15] G.X. Song, L.W. Wang, R.Q. Yang, Y.C. Ji, R.T. Zhang, L. Yang, L.H. Ding, A.Z. Wang, N. Ren, and X. Yu, Enhanced antibacterial photocatalytic activity of porous few-layer C_3N_4, *J. Nanosci. Nanotechnol.*, 20(2020), No. 9, p. 5944.

[16] T. Hisatomi, J. Kubota, and K. Domen, Recent advances in semiconductors for photocatalytic and photoelectrochemical water splitting, *Chem. Soc. Rev.*, 43(2014), No. 22, p. 7520.

[17] Z.K. Yue, A.J. Liu, C.Y. Zhang, J. Huang, M.S. Zhu, Y.K. Du, and P. Yang, Noble-metal-free hetero-structural CdS/Nb_2O_5/N-doped-graphene ternary photocatalytic system as visible-light-driven photocatalyst for hydrogen evolution, *Appl. Catal. B*, 201(2017), p. 202.

[18] X. Yu, Z.H. Zhao, D.H. Sun, N. Ren, L.H. Ding, R.Q. Yang, Y.C. Ji, L.L. Li, and H. Liu, TiO_2/TiN core/shell nanobelts for efficient solar hydrogen generation, *Chem. Commun.*, 54(2018), No. 47, p. 6056.

[19] X. Yu, Z.H. Zhao, N. Ren, J. Liu, D.H. Sun, L.H. Ding, and H. Liu, Top or bottom, assembling modules determine the photocatlytic property of the sheetlike nanostructured hybrid photocatalyst composed with Sn_3O_4 and rGO (GQD), *ACS Sustainable Chem. Eng.*, 6(2018), No. 9, p. 11775.

[20] D.D. Li, S.H. Yu, and H.L. Jiang, From UV to near-infrared light-responsive metal−organic framework composites: Plasmon and upconversion enhanced photocatalysis, *Adv. Mater.*, 30(2018), No. 27, art. No. 1707377.

[21] X. Cheng, Y.J. Zhang, and Y.P. Bi, Spatial dual-electric fields for highly enhanced the solar water splitting of TiO_2 nanotube arrays, *Nano Energy*, 57(2019), p. 542.

[22] Z.R. Liu, L.W. Wang, X. Yu, J. Zhang, R.Q. Yang, X.D. Zhang, Y.C. Ji, M.Q. Wu, L. Deng, L.L. Li, and Z.L. Wang, Piezoelectric-effect-enhanced full-spectrum photoelectrocatalysis in p−n heterojunction, *Adv. Funct. Mater.*, 29(2019), No. 41, art. No. 1807279.

[23] L.M. Sun, R. Li, W.W. Zhan, Y.S. Yuan, X.J. Wang, X.G. Han, and Y.L. Zhao, Double-shelled hollow rods assembled from nitrogen/sulfur-codoped carbon coated indium oxide nanoparticles as excellent photocatalysts, *Nat. Commun.*, 10(2019), art. No. 2270.

[24] Y.J. Wang, Q.S. Wang, X.Y. Zhan, F.M. Wang, M. Safdar, and J. He, Visible light driven type Ⅱ heterostructures and their en-

hanced photocatalysis properties: A review, *Nanoscale*, 5(2013), No. 18, p. 8326.

[25] Z.R. Liu, X. Yu, and L.L. Li, Piezopotential augmented photo- and photoelectro-catalysis with a built-in electric field, *Chin. J. Catal.*, 41(2020), No. 4, p. 534.

[26] H. Esmaili, A. Kotobi, S. Sheibani, and F. Rashchi, Photocatalytic degradation of methylene blue by nanostructured Fe/FeS powder under visible light, *Int. J. Miner. Metall. Mater.*, 25(2018), No. 2, p. 244.

[27] C.M. Ding, J.Y. Shi, Z.L. Wang, and C. Li, Photoelectrocatalytic water splitting: Significance of cocatalysts, electrolyte, and interfaces, *ACS Catal.*, 7(2017), No. 1, p. 675.

[28] X.F. Li, X.B. Meng, J. Liu, D.S. Geng, Y. Zhang, M.N. Banis, Y.L. Li, J.L. Yang, R.Y. Li, X.L. Sun, M. Cai, and M.W. Verbrugge, Tin oxide with controlled morphology and crystallinity by atomic layer deposition onto graphene nanosheets for enhanced lithium storage, *Adv. Funct. Mater.*, 22(2012), No. 8, p. 1647.

[29] X.J. She, J.J. Wu, H. Xu, J. Zhong, Y. Wang, Y.H. Song, K.Q. Nie, Y. Liu, Y.C. Yang, M.-T.F. Rodrigues, R. Vajtai, J. Lou, D.L. Du, H.M. Li, and P.M. Ajayan, High efficiency photocatalytic water splitting using 2D α-Fe_2O_3/g-C_3N_4 Z-scheme catalysts, *Adv. Energy Mater.*, 7(2017), No. 17, art. No. 1700025.

[30] X. Yu, Z.H. Zhao, J. Zhang, W.B. Guo, L.L. Li, H. Liu, and Z.L. Wang, One-step synthesis of ultrathin nanobelts-assembled urchin-like anatase TiO_2 nanostructures for highly efficient photocatalysis, *CrystEngComm*, 19(2017), No. 1, p. 129.

[31] X. Yu, L.F. Wang, J. Zhang, W.B. Guo, Z.H. Zhao, Y. Qin, X.N. Mou, A.X. Li, and H. Liu, Hierarchical hybrid nanostructures of Sn_3O_4 on N doped TiO_2 nanotubes with enhanced photocatalytic performance, *J. Mater. Chem. A*, 3(2015), No. 37, p. 19129.

[32] R.Q. Yang, Y.C. Ji, Q. Li, Z.H. Zhao, R.T. Zhang, L.L. Liang, F. Liu, Y.K. Chen, S.W. Han, X. Yu, and H. Liu, Ultrafine Si nanowires/Sn_3O_4 nanosheets 3D hierarchical heterostructured array as a photoanode with high-efficient photoelectrocatalytic performance, *Appl. Catal. B*, 256(2019), art. No. 117798.

[33] S.D. Balgude, Y.A. Sethi, B.B. Kale, N.R. Munirathnam, D.P. Amalnerkar, and P.V. Adhyapak, Nanostructured layered Sn_3O_4 for hydrogen production and dye degradation under sunlight, *RSC Adv.*, 6(2016), No. 98, p. 95663.

[34] C.M. Li, S.Y. Yu, H.J. Dong, C.B. Liu, H.J. Wu, H.N. Che, and G. Chen, Z-scheme mesoporous photocatalyst constructed by modification of Sn_3O_4 nanoclusters on g-C_3N_4 nanosheets with improved photocatalytic performance and mechanism insight, *Appl. Catal. B*, 238(2018), p. 284.

[35] L.P. Zhu, H. Lu, D. Hao, L.L. Wang, Z.H. Wu, L.J. Wang, P. Li, and J.H. Ye, Three-dimensional lupinus-like TiO_2 nanorod@Sn_3O_4 nanosheet hierarchical heterostructured arrays as photoanode for enhanced photoelectrochemical performance, *ACS Appl. Mater. Interfaces*, 9(2017), No. 44, p. 38537.

[36] R.Q. Yang, Y.C. Ji, J. Zhang, R.T. Zhang, F. Liu, Y.K. Chen, L.L. Liang, S.W. Han, X. Yu, and H. Liu, Efficiently degradation of polyacrylamide pollution using a full spectrum Sn_3O_4 nanosheet/Ni foam heterostructure photoelectrocatalyst, *Catal. Today*, 335(2019), p. 520.

[37] B.B. Zhang, L. Wang, Y.J. Zhang, Y. Ding, and Y.P. Bi, Ultrathin FeOOH nanolayers with abundant oxygen vacancies on $BiVO_4$ photoanodes for efficient water oxidation, *Angew. Chem. Int. Ed.*, 57(2018), No. 8, p. 2248.

[38] Y.X. Zhao, Y.F. Zhao, R. Shi, B. Wang, G.I.N. Waterhouse, L.Z. Wu, C.H. Tung, and T.R. Zhang, Tuning oxygen vacancies in ultrathin TiO_2 nanosheets to boost photocatalytic nitrogen fixation up to 700 nm, *Adv. Mater.*, 31(2019), No. 16, art. No. 1806482.

[39] Y.W. Wang, F. Liu, G.R. Williams, D.B. Zhang, X.G. Kong, and X.D. Lei, Enhancing photocatalytic activity of Nb_2O_{5-x} for aerobic oxidation through synergy of oxygen vacancy and porosity, *J. Nanosci. Nanotechnol.*, 20(2020), No. 4, p. 2495.

[40] M.F. Liang, T. Borjigin, Y.H. Zhang, B.H. Liu, H. Liu, and H. Guo, Controlled assemble of hollow heterostructured g-C_3N_4@CeO_2 with rich oxygen vacancies for enhanced photocatalytic CO_2 reduction, *Appl. Catal. B*, 243(2019), p. 566.

[41] J. Bao, X.D. Zhang, B. Fan, J.J. Zhang, M. Zhou, W.L. Yang, X. Hu, H. Wang, B.C. Pan, and Y. Xie, Ultrathin spinel-structured nanosheets rich in oxygen deficiencies for enhanced electrocatalytic water oxidation, *Angew. Chem. Int. Ed.*, 54(2015), No. 25, p. 7399.

[42] C.Z. Yuan, J.Y. Li, L.R. Hou, X.G. Zhang, L.F. Shen, and X.W. Lou, Ultrathin mesoporous $NiCo_2O_4$ nanosheets supported on Ni foam as advanced electrodes for supercapacitors, *Adv. Funct. Mater.*, 22(2012), No. 21, p. 4592.

[43] H.D. She, H. Zhou, L.S. Li, L. Wang, J.W. Huang, and Q.Z. Wang, Nickel-doped excess oxygen defect titanium dioxide for efficient selective photocatalytic oxidation of benzyl alcohol, *ACS Sustainable Chem. Eng.*, 6(2018), No. 9, p. 11939.

[44] G.H. Chen, S.Z. Ji, Y.H. Sang, S.J. Chang, Y.N. Wang, P. Hao, J. Claverie, H. Liu, and G.W. Yu, Synthesis of scaly Sn_3O_4/TiO_2 nanobelt heterostructures for enhanced UV−visible light photocatalytic activity, *Nanoscale*, 7(2015), No. 7, p. 3117.

[45] X. Yu, Z.H. Zhao, D.H. Sun, N. Ren, J.H. Yu, R.Q. Yang, and H. Liu, Microwave-assisted hydrothermal synthesis of Sn_3O_4 nanosheet/rGO planar heterostructure for effcient photocatalytic hydrogen generation, *Appl. Catal. B*, 227(2018), p. 470.

[46] D.H. Nam, R.H. Kim, D.W. Han, and H.S. Kwon, Electrochemical performances of Sn anode electrodeposited on porous Cu foam for Li-ion batteries, *Electrochim. Acta*, 66(2012), p. 126.

[47] Y.H. He, D.Z. Li, J. Chen, Y. Shao, J.J. Xian, X.Z. Zheng, and P. Wang, Sn_3O_4: A novel heterovalent-tin photocatalyst with hierarchical 3D nanostructures under visible light, *RSC Adv.*, 4(2014), No. 3, p. 1266.

[48] Q.Z. Zhang, S.Y. Huang, J.J. Deng, D.T. Gangadharan, F. Yang, Z.H. Xu, G. Giorgi, M. Palummo, M. Chaker, and D.L. Ma, Ice-assisted synthesis of black phosphorus nanosheets as a metal-free photocatalyst: 2D/2D heterostructure for broadband H_2 evolution, *Adv. Funct. Mater.*, 29(2019), No. 28, art. No. 1902486.

[49] X. Yu, Z.H. Zhao, J. Zhang, W.B. Guo, J.C. Qiu, D.S. Li, Z. Li, X.N. Mou, L.L. Li, A.X. Li, and H. Liu, Rutile nanorod/anatase nanowire junction array as both sensor and power supplier for high-performance, self-powered, wireless UV photodetector, *Small*, 12(2016), No. 20, p. 2759.

[50] W.W. Xia, H.B. Wang, X.H. Zeng, J. Han, J. Zhu, M. Zhou, and S.D. Wu, High-efficiency photocatalytic activity of type Ⅱ SnO/Sn_3O_4 heterostructures via interfacial charge transfer, *CrystEngComm*, 16(2014), No. 30, p. 6841.

[51] R.C. Pawar, V. Khare, and C.S. Lee, Hybrid photocatalysts using graphitic carbon nitride/cadmium sulfide/reduced graphene oxide (g-C_3N_4/CdS/RGO) for superior photodegradation of organic pollutants under UV and visible light, *Dalton Trans.*, 43(2014), No. 33, p. 12514.